USGS
science for a changing world

Prepared for the National Aeronautics and Space Administration

Geologic Map of the Mead Quadrangle (V–21), Venus

By Bruce A. Campbell and David A. Clark

Pamphlet to accompany
Scientifiic Investigations Map 2897

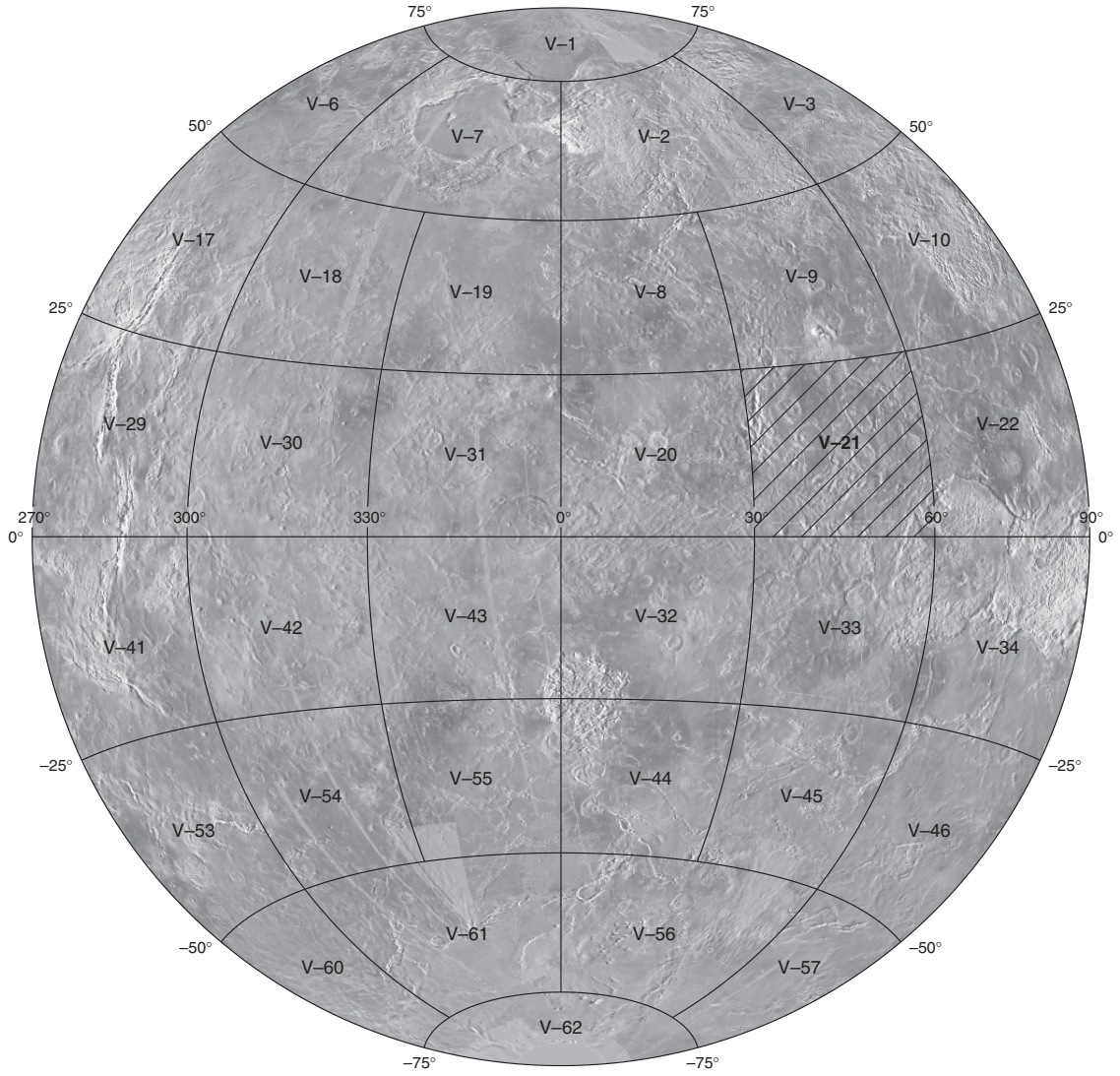

2006

U.S. Department of the Interior
U.S. Geological Survey

INTRODUCTION

THE MAGELLAN MISSION

The Magellan spacecraft orbited Venus from August 10, 1990, until it plunged into the Venusian atmosphere on October 12, 1994. Magellan Mission objectives included (1) improving the knowledge of the geological processes, surface properties, and geologic history of Venus by analysis of surface radar characteristics, topography, and morphology and (2) improving the knowledge of the geophysics of Venus by analysis of Venusian gravity.

The Magellan spacecraft carried a 12.6-cm radar system to map the surface of Venus. The transmitter and receiver systems were used to collect three data sets: (1) synthetic aperture radar (SAR) images of the surface, (2) passive microwave thermal emission observations, and (3) measurements of the backscattered power at small angles of incidence, which were processed to yield altimetric data. Radar imaging and altimetric and radiometric mapping of the Venusian surface were accomplished in mission cycles 1, 2, and 3 from September 1990 until September 1992. Ninety-eight percent of the surface was mapped with radar resolution on the order of 120 m. The SAR observations were projected to a 75-m nominal horizontal resolution, and these full-resolution data compose the image base used in geologic mapping. The primary polarization mode was horizontal-transmit, horizontal-receive (HH), but additional data for selected areas were collected for the vertical polarization sense. Incidence angles varied between about 20° and 45°.

High-resolution Doppler tracking of the spacecraft took place from September 1992 through October 1994 (mission cycles 4, 5, 6). Approximately 950 orbits of high-resolution gravity observations were obtained between September 1992 and May 1993 while Magellan was in an elliptical orbit with a periapsis near 175 km and an apoapsis near 8,000 km. An additional 1,500 orbits were obtained following orbit-circularization in mid-1993. These data exist as a 75° by 75° harmonic field.

MAGELLAN RADAR DATA

Radar backscatter power is determined by (1) the morphology of the surface at a broad range of scales and (2) the intrinsic reflectivity, or dielectric constant, of the material. Topography at scales of several meters and larger can produce quasi-specular echoes, and the strength of the return is greatest when the local surface is perpendicular to the incident beam. This type of scattering is most important at very small angles of incidence, because natural surfaces generally have few large tilted facets at high angles. The exception is in areas of steep slopes, such as ridges or rift zones, where favorably tilted terrain can produce very bright signatures in the radar image. For most other areas, diffuse echoes from roughness at scales comparable to the radar wavelength are responsible for variations in the SAR return. In either case, the echo strength is also modulated by the reflectivity of the surface material. The density of the upper few wavelengths of the surface can have a significant effect. Low-density layers, such as crater ejecta or volcanic ash, can absorb the incident energy and produce a lower observed echo. On Venus, a rapid increase in reflectivity exists at a certain critical elevation above which high-dielectric minerals or coatings are thought to be present. This leads to very bright SAR echoes from virtually all areas above that critical elevation.

The measurements of passive thermal emission from Venus, though of much lower spatial resolution than the SAR data, are more sensitive to changes in the dielectric constant of the surface than to roughness. They can be used to augment studies of the surface and to discriminate between roughness and reflectivity effects. Observations of the near-nadir backscatter power, collected using a separate smaller antenna on the spacecraft, were modeled using the Hagfors expression for echoes from gently undulating surfaces to yield estimates of planetary radius, Fresnel reflectivity, and root-mean-square (rms) slope. The topographic data produced by this technique have horizontal footprint sizes of about 10 km near periapsis and a vertical resolution on the order of 100 m. The Fresnel reflectivity data provide a comparison to the emissivity maps, and the rms slope parameter is an indicator of the surface tilts, which contribute to the quasi-specular scattering component.

MEAD QUADRANGLE

The Mead quadrangle (V–21) of Venus is bounded by lat 0° and 25° N., long 30° and 60° E. This quadrangle is one of 62 covering Venus at 1:5,000,000 scale. Named for the largest crater on Venus, the quadrangle is dominated by effusive volcanic deposits associated with five major coronae in eastern Eistla Regio (Didilia, Pavlova, Calakomana, Isong, and Ninmah), corona-like tectonic features, and Disani Corona (fig. 1*A*). The southern extremity of Bell Regio, marked by lava flows from Nyx Mons, north of the map area, forms the north-central part of the quadrangle. The shield volcanoes Kali, Dzalarhons, and Ptesanwi Montes lie south and southwest of the large corona-related flow field. Lava flows from sources east of Mead crater flood low-lying areas along the east edge of the quadrangle.

The predominantly smooth volcanic plains of Akhtamar Planitia form the background terrain. The highest locations in eastern Eistla Regio are almost 4 km above the planetary datum radius of 6,051 km, but the average elevation across this broad rise is 1–2 km (fig. 1*B*). The surrounding plains are typically within 1 km of the datum. Near the crater Orczy (lat 3.7° N., long 52.3° E.) is a network of anastomosing channels (Ganga Valles*) that incise the regional plains. Mead crater, approximately 270 km in diameter, lies near the east edge of the map region. An additional 14 impact craters are identified within the quadrangle.

Tectonic deformation within the quadrangle produced a network of wrinkle ridges in the regional plains material. The density of these ridges varies across the map region (for example, Bilotti and Suppe, 1999). Greater degrees of deformation

*Name provisionally accepted by International Astronomical Union

are associated with uplifted corona rims, a belt of ridges in the northwestern portion of the quadrangle (Metelitsa Dorsa), and a relatively small ridge complex, Ojuz Dorsa, that links Mafdet and Gbadu Tesserae. The central regions of individual coronae are characterized by densely lineated, stellate or wishbone-shaped features. Relatively small outcrops of heavily deformed terrain occur within the plains units (Mamitu, Salus, Vako-nana, Mafdet, and Gbadu Tesserae), and the southeastern portion of the quadrangle contains the outlying highlands of western Ovda Regio (Manatum Tessera).

Previous work focused on the distribution and morphology of the coronae (quasi-circular features displaying a wide range of annular rim structures, exterior deformation, and associated volcanism) within eastern Eistla Regio as part of global statistical studies (Stofan and others, 1992). Detailed geologic mapping of coronae elsewhere on Venus includes a study by Copp and others (1998), which shows that corona-related volcanism may have been punctuated by periods of tectonic deformation; our results support this broad premise. McGill (1994) found that coronae in central Eistla Regio (quadrangle V–20, immediately west of the map region) are stratigraphically older than nearby major shield volcanoes, which suggests a thickening of the local lithosphere with time. In studies of Bell Regio (quadrangle V–9, immediately north of the map region), Campbell and Campbell (2002) and Campbell and Rogers (1994) note a similar progression from coronalike features to steep-sided shield volcanoes, with inferred increasing lithospheric thickness (Rogers and Zuber, 1998). Four of the major coronae in eastern Eistla Regio have distinguishable gravity anomalies (Zimmerman and Johnson, 2000), as do the two corona-volcano hybrid structures in central Eistla Regio, Irnini and Anala Montes (McGill, 1998, 2000). These gravity anomalies indicate that corona topography is not fully compensated, implying possible dynamic support (for example, mantle plumes).

Mead crater was studied by Schaber and others (1992) and Herrick and Sharpton (1996). These authors differ slightly in their interpretation of the radar-dark materials surrounding Mead; Schaber and others (1992) propose that the dark material is related to impact-triggered volcanism, while Herrick and Sharpton (1996) suggest that it is composed of plains volcanic material that embays the crater ejecta blanket. Our mapping supports the latter hypothesis, though the sources for the embaying material include sources east, west, and north of the crater. The Mead crater floor may consist of a layer of impact melt emplaced immediately after crater excavation, with subsequent modest tectonic deformation, or a post-impact volcanic deposit (Herrick and Sharpton, 1996). Weitz (1993) and Campbell (1994) discuss the backscatter and emissivity properties of the Mead crater floor and note a minor but distinct shift in dielectric constant from east to west. Mead impact ejecta is also the likely source of fine-grained, radar-dark materials that mantle large areas in the southeastern region of the quadrangle. This material is preferentially concentrated in local areas of low elevation, and high-standing areas show evidence for progressive stripping (presumably aeolian) of an originally more extensive mantling layer.

Eastern Eistla Regio is of interest for the large-scale volcanism associated with the coronae and corona-like deformation features. The geologic history of this region appears to be significantly different from that delineated for Bell Regio (Campbell and Campbell, 2002) in the lack of relatively young, steep-sided volcanic constructs such as Tepev Mons and Otafuku Tholi in V–9. There are similarities, however, between the initial stages of volcanism at Bell Regio, associated with the corona-like Nyx Mons just north of the map area, and the sheet-like flow aprons of the coronae of eastern Eistla Regio. Despite the lack of steep-sided constructs, several of the coronae in the Mead quadrangle have associated radar-bright deposits that we interpret to be pyroclastic materials. There is evidence in both regions for a broad range of volcanic processes, perhaps including more evolved magmas over time, but the differences between these two adjacent highland rises offers an opportunity to characterize the distinctive features of corona- and shield-related materials.

METHODS AND DATA

This geologic map was compiled from Magellan radar images at a base resolution of approximately 260 m/pixel. The resampled (75 m/pixel) F-MAP data were used to check unit contacts and to identify subtle or small features. Most of the quadrangle lies within the superior conjunction gap of the first Magellan mapping cycle, so the left-looking image data were collected primarily during cycle 2. These data have radar incidence angles of 44°–46°. The eastern and northern parts of the quadrangle were covered by Magellan cycle 3 right-looking stereo observations, with incidence angles of approximately 25°. These data were used to distinguish the relief of tectonic features surrounding Mead crater and to extend the incidence-angle range of surface property descriptions. Altimetry data were derived from both resampled topographic maps having 5.4 km horizontal resolution and from analysis of individual Magellan altimeter footprint records (Ford and Pettengill, 1992; Campbell and others, 1999). Magellan emissivity (fig. 2*A*), rms slope (fig. 2*B*), and Fresnel reflectivity data provide valuable additional information on the presence and nature of surficial deposits.

Unit boundaries in the geologic map were defined primarily on the basis of changes in surface morphology inferred from the radar data. The mapped units are shown within a tentative relative age sequence, based on superposition and cross-cutting relations, in the Correlation of Map Units and Major Events (map sheet). Radar backscatter strength at incidence angles of 44°–46° is controlled largely by the wavelength-scale roughness of the surface. Below 6,054 km radius, variations in the bulk dielectric constant are a minor contributor to the surface backscatter coefficient, unless there is a significant depth of fine-grained mantling material. Above this elevation, however, surface-atmosphere interactions produce highly reflective terrain for which roughness is a secondary factor in the backscattered return (Campbell, 1995; Campbell and others, 1999). Magellan ancillary data on surface emissivity and reflectivity were used to further constrain surface unit properties.

STRATIGRAPHY

The stratigraphic units in the Mead quadrangle are grouped by major geographic province: western Ovda Regio, which forms the southern portion of the quadrangle; eastern Eistla Regio; and southern Bell Regio, which forms the north-central portion of the quadrangle. A separate group comprises widespread units: tessera (unit t), regional plains (unit pr), and impact craters (units cu and co). For each province, we present a correlation chart of the major units. This approach avoids the implication that, for example, localized homogeneous plains units across the map form a common time-stratigraphic horizon. Within the three provinces, we identify densely lineated materials (unit ld); flow materials of central volcanoes, localized sources, and coronae (unit names beginning with f); radar-bright halo materials (unit hb); and localized plains materials (unit names beginning with p). Materials related to Mead crater are mapped as distinct units (names beginning with cM) within the eastern Eistla Regio province. Surficial materials are shown as a stippled pattern. Unit names are chosen to identify each unit by its primary characteristics or to show association with a major geomorphic feature. Quantitative backscatter and ancillary data for type areas of mapped units are presented in table 1, and the relative backscatter properties of selected major units are presented in a comparison with radar data for terrestrial lava flows in figure 3.

WIDESPREAD TESSERA AND PLAINS MATERIAL

The oldest exposed unit at any locale in the quadrangle forms complex ridged terrain called tessera material (unit t). All tesserae are embayed by plains units and (or) corona/edifice lava flows. In general, there is not agreement as to whether or not tesserae constitute a global time-stratigraphic marker (Basilevsky and Head, 1998; Guest and Stofan, 1999). In the Mead quadrangle, however, continuity of structural patterns between outcrops of tessera material separated by as much as 1,000 km strongly suggests a common period of deformation. For example, the trend and deformation pattern within Mafdet Tessera are very similar to those of Mamitu Tesserae, which extends northward into Bell Regio. Mafdet Tessera, in turn, appears to be an extension of Gbadu Tessera. This suggests a possible early, more extensive tessera fabric across the regions that has subsequently been largely buried by volcanic materials. As a result, we have not differentiated the tessera materials among the three geographic provinces, and we suggest that they are similar in at least the age of their last major deformational period. Their actual age of formation as elevated terrain and the nature of the original surface material are indeterminate.

Regional plains material surrounding eastern Eistla Regio is mapped as a single unit (unit pr). A dense network of wrinkle ridges and annular tectonic patterns deforms unit pr. We also included the annular materials of Calakomana Corona within this unit, because the density of fractures and ridges in the bounding structures is much less than that found at Didilia and Pavlova Coronae and other coronae in eastern Eistla Regio. Where not affected by tectonic deformation, the surface is smooth at both the hundreds of meters scale (1°–3° rms slope) and the centimeter scale (low 12.6-cm-radar cross section: table 1). We interpret the regional plains material to have originated as the result of extensive flooding by low-viscosity (for example, basaltic) volcanic material. The regional plains material in quadrangle V–9 (Campbell and Campbell, 2002) is subdivided into two units based on the density of superposed tectonic deformation (wrinkle ridges). Because this division is not based on properties of the original rock units, we do not make the same distinction in V–21.

WESTERN OVDA REGIO MATERIAL

We map as individual units the flow materials of Dzalarhons Mons, including Nekhebet Fluctus (unit fD) and Ptesanwi Mons (unit fP), which form aprons of lobate flows that trend radial to the respective volcano center, superpose the regional plains (unit pr), and, in some locales, embay tessera materials (unit t). Based on apparent topographic control of flow direction, we infer that Ptesanwi Mons postdates the uplift of Calakomana Corona.

Homogenous plains material of Ovda Regio (unit phO) occurs in the southeast portion of the quadrangle, superposes the regional plains material (unit pr), and embays Salus and Manatum Tesserae. Unit phO likely comprises contributions from a number of sources, including Verdandi Corona (southeast of the map region), Disani Corona, and a region of abundant small shields and pit crater chains northeast of Orczy crater (fig. 4). Unit phO is characterized by homogeneous radar image texture, low rms slope, and moderate to low radar backscatter (table 1). These properties suggest a smooth surface at scales ranging from centimeters to hundreds of meters.

Channel structures are common in the portion of Ovda Regio within V–21. A narrow, sinuous, anastomosing channel system (Ganga Valles*) extends northeast about 200 km from Orczy crater, which likely masks the source vent. A channel farther to the northeast of Orczy is wider and has been partially flooded and buried by later volcanic materials (fig. 4). We infer these channels were formed by thermal and mechanical erosion caused by flowing lava and are incised only into regional plains material of unit pr. Materials of units phO and fc truncate or embay the channels, filling areas of low elevation. These later materials likely superpose any distal outflow deposits associated with the channel-forming eruptions. A channel that exploited pre-existing graben structures occurs in the north-central portion of Disani Corona (fig. 5), and we infer this channel formed contemporaneously with the surrounding material of unit phO.

EASTERN EISTLA REGIO MATERIAL

Densely lineated material (unit ld) forms primarily the center and annular bounding terrain of coronae and is characterized by dense patterns of tectonic deformation with a single dominant trend; for the annular features, this trend is often radial to the corona center. While the tectonic deformation is often so pervasive as to preclude inference of the pre-existing surface properties, these outcrops are sufficiently

distinct from tessera and plains materials to warrant mapping as a discrete unit. In the center of each corona is an area of elevated, densely lineated material (fig. 6). These central features range from stellate (Pavlova Corona) to linear or wish-bone shaped (Didilia and Isong Coronae). There are also apparent remnants of corona center structures southwest and east of Pavlova Corona and southeast of Isong Corona. Materials of unit fc embay the densely lineated material and superpose the regional plains, so we infer that the densely lineated materials are older than the surrounding flows. Whether unit ld consists of highly deformed regional plains material (unit pr) or older terrain embayed by the regional plains is uncertain. We indicate this uncertainty by an overlap of the relative age ranges of unit ld and unit pr in the Correlation of Map Units and Major Events (map sheet). We also suggest that variations in extant corona structures reflect varying degrees of subsidence and burial by unit fc. A correlation between structural preservation and corona age is speculative, but we indicate a possible overlap in age for unit ld relative to flow materials of coronae (unit fc) in the Correlation of Map Units and Major Events.

In the plains surrounding eastern Eistla Regio, localized flow materials (unit fl) of moderate to bright radar return surround low-relief shield volcanoes or caldera-like depressions. There is also a large flow field associated with Ojuz Dorsa. While mapped as a single unit, we make no inference about the relative age of these isolated flow fields. All of these flow complexes superpose the regional plains (unit pr) and, in some locales, embay tessera materials (unit t) or densely lineated material (unit ld). Where the contacts can be distinguished, north and northwest of Didilia Corona, corona flow materials (unit fc) appear to superpose the localized flow materials (unit fl).

The central rise of eastern Eistla Regio is covered by volcanic flows associated with the major coronae and a number of structural features that may be corona remnants. Because the distal lobate margins of flow complexes are discontinuous, we map the deposits as flow material of coronae (unit fc), which covers an area of approximately 2.2×10^6 km^2. Two distinct flow complexes are mapped as flow materials of Calakomana Corona (unit fC). Despite the lack of clear boundaries between most flow complexes associated with the major coronae, the area north of Pavlova Corona offers an example of the general stratigraphic succession (fig. 7). There is a distinct contact between older Pavlova Corona flow material and younger deposits from Didilia Corona that are deflected by higher-standing flow margins. At least in this region, the older flow units from both coronae are lobate, radar bright, relatively narrow, and frequently exhibit central channels. Younger flows are more sheetlike and radar dark and have diffuse distal contacts with the surrounding plains. The younger flows superpose lower-standing areas of the radar-bright flow lobes and appear to flood some channels. As a result, the distal margins of unit fc northeast of Didilia and Pavlova Coronae are characterized by a combination of feathery, radar-dark terrain and the remnant portions of partially buried, rough lobate flows. In contrast, the later flows of Nyx Mons (unit fN_3) are more radar bright than the preceding sheet-like deposits (unit fN_1).

Lobate, radar-bright flows are typically associated with high-volume eruption rates (rapid overturn of lava surface crusts) or increased magma viscosity. Sheetlike, low-return materials are likely produced by low eruption rates (tube fed or slowly inflated deposits) or by less viscous magma. The progression in lava flow morphology observed for Pavlova and Didilia Coronae implies a complex history of magma sources, compositions, and (or) eruption rates.

Flow material of Kali Mons (unit fK) forms an apron of lobate flows that trends radial to the volcano center, superposes the regional plains, and, in some locales, embays tessera deposits. The radiophysical properties of most edifice flows are consistent across the quadrangle. Where the radar backscatter is enhanced, we observe moderate to slightly enhanced emissivity, consistent with a surface that is rougher at the wavelength scale than the surrounding plains (Campbell, 1995). Where the backscatter is low, the emissivity is correspondingly lower than the planetary average. There is, however, a distinctive area of higher emissivity correlated with low-radar-return lava flows from Kali Mons (fig. 2*A*, fig. 8). Small patches of enhanced emissivity are also associated with radar-dark units in Calakomana Corona. Enhanced emissivity is indicative of either an increased wavelength-scale roughness or a lower bulk dielectric constant. Since the lava flows are radar dark, the former explanation is untenable. The likely reason for such behavior is a low bulk density, due either to a surficial mantling layer or an intrinsic property of the lava flows (for example, high vesicularity). While a low-density pyroclastic mantling deposit could also exhibit these properties, it seems unlikely that such a deposit would be confined to the area of a single flow complex.

Mead crater and its associated deposits represent a significant time-stratigraphic marker for the eastern portion of the map region. Mead crater is considerably more complex than other craters in the quadrangle. Following previous studies (Schaber and others, 1992; Herrick and Sharpton, 1996), we mapped as separate units crater floor material (unit cMf), terrace material (unit cMt), and distal ejecta material (unit cMu) of Mead crater. The crater floor exhibits an interesting dichotomy in surface properties; emissivity data (fig. 9) suggest that the southeastern portion has a dielectric constant of 4–5 (close to the planetary average of 4.2), while the remainder of the crater floor is characterized by values of 7–8 (Weitz, 1993; Campbell, 1994). The crater floor material, which likely formed as either an impact melt sheet or post-emplacement volcanic deposit, is characterized by a modest but abrupt shift in chemical or physical properties. It is interesting that no significant areas with decreased emissivity are observed in the Mead crater terrace region or proximal ejecta blanket. If the low-emissivity floor material is composed of impact melt, it suggests some combination of minimal melt ejection and (or) rapid drainage of any exterior deposits into the crater cavity. The uncertainty in the duration of floor material emplacement is reflected in the Correlation of Map Units and Major Events (map sheet).

The distal ejecta deposits of Mead crater are much less radially extensive than might be expected for a pristine, large

crater. Even in the dense atmosphere, primary and secondary ejecta features should form a more complete annulus around the rim. This discontinuous primary ejecta pattern suggested to previous workers the embayment of the initial ejecta blanket by flow materials. We divide the radar-dark deposits surrounding Mead crater into flow material of coronae (unit fc) and flow material near Mead crater (unit fM), which is likely related to a chain of small edifices northeast of the crater and a volcanic center near lat 14° N., long 64.5° E. We mapped a short north-trending channel structure just north of Mead crater, which may also be associated with the emplacement of unit fM. Contacts between the two embaying units are difficult to trace, and we used the local topographic relief and degree of burial of tectonic structures to infer a contact. The materials of both units superpose unit pr, as evidenced by the absence of wrinkle ridges in areas of low topography (fig. 10). High-standing arcuate ridges surround the crater along all but the southwest corner and confine the erupted material.

Within eastern Eistla Regio are at least seven distinct areas of very high radar backscatter, mapped as bright halo material (unit hb). These areas occur adjacent to densely lineated material (unit ld), are characterized by feathery edges and minimal internal features, and mantle pre-existing lava flows from the coronae (fig. 11). There is little evidence for spatial variability in deposit depth or roughness, with the exception of small oval or linear regions of enhanced backscatter. Based on backscatter and emissivity data, unit hb deposits are interpreted to be coarse-grained (particle sizes greater than a few centimeters) mantling material emplaced by pyroclastic volcanic activity (Campbell and others, 1998). The lack of apparent sorting of the material precludes identification of a likely source for each deposit, though a surge driven by a collapsing eruption column would travel primarily downslope. Radar-dark wind streaks are observed along the margins of some deposits of unit hb, suggesting that the total relief within the rough terrain is on the order of perhaps tens of centimeters to permit burial by the thin wind-borne material. McGill (1994) identified similar, but more extensive, deposits on Anala and Irnini Montes in the adjacent V–20 quadrangle.

Within V–21, the radar-bright areas occur on the west side of densely lineated materials that form corona rim deposits (unit ld). This might suggest some control of deposition by prevailing east-west winds, but the similar deposits in central Eistla Regio are concentric to Anala and Irnini Montes. It is also possible that the bright radar echoes are due to a micro-dune structure on scales below the resolution of the Magellan radar images rather than to a jumbled surface of small pyroclastic fragments. Where such deposits have been identified on Venus, they are associated with a nearby impact crater (for example, Guan Daosheng crater near lat 61.1° S., long 181.8° E.). The radar-bright materials in central and eastern Eistla Regio are not clearly linked to impact crater deposits.

SOUTHERN BELL REGIO MATERIAL

In the northwestern portion of the quadrangle, low-radar-return regions resemble terrain mapped as smooth plains material in the Bell Regio quadrangle (V–9). In V–21, however, the radar-dark materials do not have distinct lobate margins, and, in some locales, they form wind streaks associated with topographic gaps in tessera units. The low-radar return in this portion of the quadrangle appears to be due to a combination of surficial mantling material (possibly from Corinna crater) and relatively smooth plains-forming and corona flow materials.

The Homogeneous plains material of Bell Regio (unit phB) is characterized by relatively homogeneous radar-image texture, subdues pre-existing terrain features such as wrinkle ridges, and superposes unit pr. Unit phB is also characterized by enhanced backscatter and emissivity relative to unit pr (fig. 2), suggesting a rougher texture at the 12.6-cm scale. McGill (2000) mapped similar plains-forming material as homogeneous plains material in quadrangle V–20.

Flow material of Nyx Mons (units fN_1 and fN_3) extend south into the topographic low between Bell and eastern Eistla Regiones. The oldest (fN_1) and youngest (fN_3) of these deposits occur within the Mead quadrangle; unit fN_2 is present only in quadrangle V–9. The lower flow material of Nyx Mons (unit fN_1) forms a moderate- to low-radar-return field of flows that superpose unit pr, extending radially as far as 600 km from the center of the edifice. The upper flow material of Nyx Mons (unit fN_3) forms a prominent aggregate of radar-bright flows to the south and southwest of Tepev Mons (V–9). To the south and southeast of Tepev Mons, these bright flows are superposed on unit fN_1.

WIDESPREAD IMPACT CRATER MATERIAL

A total of 15 craters occur within the V–21 quadrangle. We divide the impact crater material for all but Mead crater into two categories: crater material, undifferentiated (unit cu), comprising material of crater rims, floors, and ejecta blankets and crater outflow material (unit co). The paucity of craters across the quadrangle offers little useful information about relative unit ages (Campbell, 1999). Underscoring this point, a majority of the craters within V–21 occur on units fc and phO, which are inferred to be younger than the regional plains (unit pr), and none occur on the presumably older tesserae (unit t). There is also no evidence for a sub-population of embayed craters other than Mead crater.

Craters within the quadrangle do not exhibit large outflow deposits, but small outflows are mapped for Karo and Bradstreet craters. Outflows at Huarei and de Ayala craters are too small to be represented clearly at the 1:5,000,000 scale. Crater floors vary in radar return from very bright (for example, de Ayala) to dark (for example, Orczy). The bright floors are likely rough due to emplacement of a fractured impact melt sheet, whereas the dark floors may reflect post-excavation flooding by volcanic materials or a smooth melt sheet.

Farida crater is of interest for its associated parabolic halo of fine-grained debris, which forms an arc to the south of the crater. The ejecta blanket of Farida is also concentrated to the south, suggesting an oblique impact event. Ayashe crater, which straddles a boundary between older regional plains material (unit pr) and younger, radar-bright homogeneous plains mate-

rial (unit phB), appears at first to contradict this stratigraphy: the ejecta blanket of Ayashe is evident only on the younger plains material. We suggest that this was an oblique impact postdating both plains regions and leading to an asymmetric ejecta pattern.

SURFICIAL MATERIAL

We infer that surficial deposits in the Mead quadrangle are predominantly of impact origin and represent thin (a plausible range is on the order of 10 cm to a meter or more) layers of fine-grained material that reduce the radar echo by smoothing the surface and lowering the effective reflectivity. The primary source of these fine materials was the Mead crater impact. Major deposits of surface mantling material occur northeast and southwest of Mead crater and mantle materials of units pr and fc. Quasi-circular deposits south and northwest of Mead crater appear to be due to younger impact splotches. The mantling deposits are evident in the emissivity data as subtle lows relative to the average plains behavior (fig. 2*A*) and form distinct patches of low rms slope (fig. 2*B*).

A comparison of the Magellan radar, emissivity, and rms slope measurements with altimetry data suggests a high degree of correlation between the mantling materials and areas of low elevation. In some of these low-lying areas, the radar-dark material exhibits lobate margins that conform to subtle topographic relief, such as wrinkle ridges (fig. 12). This suggests that the initial emplacement of the mantling material may have been characterized by fluid behavior rather than solely by an airfall mechanism. Areas of locally high topography tend to be more radar bright, and radar-dark wind streaks or yardangs trend downslope from small patches of high-standing mantled terrain. The prevailing winds also produce accumulations of radar-dark material along the east sides of many wrinkle ridges. We infer that the mantling material was originally much more extensive and is being progressively stripped from high-standing terrain and redeposited in low areas. This aeolian transport of material, in many cases, appears to progress from east to west (consistent with the prevailing winds), but, in some locales, the wind regime appears to be controlled by local topography. For example, there are very distinct arcuate radar-dark wind streaks on unit fM southeast of Mead crater that appear to arise from small, radar-dark accumulations of fine material on old, high-standing ridges to the north.

Based on the evidence for lateral transport of the Mead-related mantling material, these deposits do not represent a reliable stratigraphic marker, but we examined the implications of their observed distribution. We inferred that materials of unit fc and fM embay the Mead crater ejecta blanket. There are no extensive occurrences of mantling deposits on unit fM, so our conclusions appear to be consistent. There are, however, considerable mantling deposits on portions of unit fc located southeast of Isong Corona. We must, therefore, leave open the possibility that some of the corona-related flows predate the Mead crater impact.

The physical nature, inferred from radar backscatter and emission properties, of the mantling material is intriguing. In general, fine-grained deposits are expected to have lower bulk density than a rock of the same composition and, in turn, a lower dielectric constant and enhanced emissivity. For the low-return material in V–21, we observe a slight decrease in emissivity. While this is consistent with smooth terrain, it suggests that the bulk dielectric constant of the mantling material also may be higher than that of the underlying plains (Campbell, 1994). We speculate that the fine-grained ejecta and low-emissivity material of the Mead crater floor are related in their mode of formation (for example, impact melting).

STRUCTURE

Tessera materials are characterized by multiple sets of subperpendicular tectonic deformation patterns, including ridges, grabens, or ribbon structures. Within the Mead quadrangle, the outcrops of tessera material are principally related to the equatorial highlands (Ovda Regio) and to a possibly related set of elongate outcrops that trend approximately northeast from Dzalarhons Mons past Tepev Mons to the north in quadrangle V–9. As noted above, the deformation pattern within Mafdet Tessera is similar to that of Mamitu Tesserae, which extend northward into Bell Regio. Mafdet Tessera, in turn, appears to be an extension of Gbadu Tessera. This suggests a possible early, more extensive tessera fabric across both regions that has subsequently been largely buried by volcanic materials.

The plains material (unit pr) surrounding eastern Eistla Regio is deformed by wrinkle ridges, ridge belts, and corona structures whose topographic expression limits the lateral extent of corona flows (unit fc). To the west, northeast, and south of the corona cluster, belts of closely spaced ridges form topographic highs against which these lava flows terminate. To the west, this high topography forms Metelitsa Dorsa. The southern topographic high is associated with the annular tectonic deformation of Calakomana Corona. Virtually all of this deformation appears to predate the emplacement of flow materials from Pavlova, Didilia, Isong, and Ninmah Coronae, because only a few wrinkle ridges occur within unit fc. To the north, the radial extent of unit fc is limited by low-relief wrinkle ridges and the broad topographic low in Akhtamar Planitia between Bell and Eistla Regiones. Southeast and southwest of the coronae, volcanic flows are less confined and spread onto the ridged plains and into the topographic lows surrounding Mead crater.

Bilotti and Suppe (1999) mapped wrinkle-ridge patterns across Venus and noted that the geoid high near Pavlova Corona appears to be the center of a circumferential deformation pattern approximately 3,200 km in diameter. Their analysis of other geoid highs suggests that ring-like patterns of wrinkle ridges are associated with compressional deformation in the lowlands surrounding regional uplifts. While this mechanism may explain some of the circumferential wrinkle ridges in the plains surrounding eastern Eistla Regio, gravity sliding at the margins of a broad 1–2-km-diameter rise seems unlikely to produce the densely spaced ridge belts that surround the corona complex. The origin of these ridge belts is therefore uncertain, but we infer that they record a period of

compressive tectonism (either regional or associated with rise formation) that predates the formation of structures and flows related to Didilia, Pavlova, Isong, and Ninmah Coronae.

The stress fields related to the deformation of the densely lineated material forming coronae center features (unit ld) appear unrelated to those associated with nearby belts of ridges. For example, the outcrop of unit ld southwest of Pavlova Corona has an approximately orthogonal trend to that of Metelitsa Dorsa. The densely lineated material is also characterized by extensional fractures, as well as possible compressional tectonic features. Coupled with the superposition of unit fc on the plains material and the evident topographic control of corona flow material margins, it appears that the ridge belts predate both the effusive volcanism associated with the coronae and the tectonic deformation of their central regions. If the ridge belts represent some combination of regional tectonism and a response to the formation of the rise, then the current corona features reflect later, and more localized, stress regimes. Evidence of the initial effects of the uplift in the center of eastern Eistla Regio are obscured by subsequent volcanism and tectonism.

The four major coronae of eastern Eistla Regio (Didilia, Pavlova, Ninmah, and Isong) have relatively similar structures: an uplifted, concentric outer rim; a relatively flat interior floor; and a central dome or ridge (fig. 1*B*). In contrast, Calakomana Corona has a discontinuous, less deformed outer rim, and the floor comprises a group of depressions separated by low domes or ridges. The deformation at Calakomana predates the volcanism associated with the coronae of the central rise, so the topography may reflect subsidence with increased age and withdrawal of dynamic support.

Within the eastern Eistla Regio flow complex, swarms of radar-bright lineaments, interpreted to be fractures, superpose and surround the highly deformed terrain of each corona (fig. 13). Most are radial to the major topographic expression of the nearest corona, though, in some instances, the deformation patterns of multiple coronae overlap. These fractures extend into the plains, indicating that the associated stress regime postdates the formation of the regional wrinkle ridge patterns. Fractures associated with Pavlova Corona are concentrated in areas of high topography, suggesting that old fractures along the corona flanks have been buried by later lava flows. Fractures associated with Didilia Corona cut both the elevated areas and the flank deposits. This suggests that corona uplift and volcanism were contemporaneous, or interleaved in time, at Didilia. Some fractures are associated with isolated outcrops of densely lineated material (unit ld), such as southeast of Isong Corona and southwest of Pavlova Corona. This suggests that these fractures mark the remnant structures of coronae that have been largely buried by later lava flows.

GEOLOGIC SUMMARY

The earliest geologic event within the Mead quadrangle, as elsewhere on Venus, is the development of tessera material (unit t) that is preserved as isolated patches of originally more extensive, possibly contiguous units. In particular, Mafdet and Mamitu Tesserae appear to share many similar attributes and may be associated with Gbadu Tessera, which suggests a possible early, more extensive tessera fabric linking Bell and eastern Eistla Regiones. Regional plains materials, interpreted as sheet- or flood-like volcanic flows, embay and superpose the tesserae.

The regional plains material (unit pr) later underwent widespread tectonic deformation, creating belts of densely spaced wrinkle ridges that constrain the radial extent of corona flow materials. If this deformation reflects a response to the uplift of eastern Eistla Regio (Bilotti and Suppe, 1999), then any record of this period within the central corona-dominated region has been obscured by later volcanism and tectonism. The ridge-forming deformation was contemporaneous with, or closely followed by, the uplift of Calakomana Corona. Based on its association with the circumferential ridge-belt structures and the topographic subsidence of its central region, we infer that Calakomana Corona predates the other large coronae of eastern Eistla Regio.

The post-plains-emplacement geologic history of eastern Eistla Regio is similar to the early phases of volcanism in Bell Regio. The volcanic deposits of some coronae in eastern Eistla Regio resemble the broad apron of flows surrounding Nyx Mons, which also has a wishbone-shaped central feature (V–9) similar to outcrops of unit ld in V–21. Effusive volcanism centered on the coronae in eastern Eistla Regio is interleaved in time with tectonic deformation associated with the formation of the rim materials, and remnant central structures and radial fractures suggest that earlier coronae have been buried by a combination of subsidence and volcanic embayment.

These combined observations suggest multiple periods of local corona uplift, volcanism, subsidence, and burial. If the average thickness of lava flows within unit fc is 10 m, a relatively low mass eruption rate of 10 m^3/s could emplace these materials in less than 10^5 yr. This is a minimum estimate for the duration of volcanism, because the corona-related deposits may be considerably thicker. We cannot define a clear age progression for the major coronae in the region, but the latest surface flows of Didilia Corona appear to postdate those of Pavlova Corona. Tectonic deformation, in the form of radial fractures, also appears to be more recent at Didilia Corona.

In eastern Eistla Regio, the period of corona-related volcanism is not followed by the development of progressively steeper shield volcanoes such as Tepev Mons and Otafuku Tholi in V–9. Instead, the most recent mapped phase of volcanism includes material erupted from vents located along the corona rims (unit hb). We infer that materials of unit hb formed as pyroclastic flows of coarse material produced during eruptions of volatile-rich magma along the margins of corona structures. There is little evidence for sorting of the debris with increasing distance from the apparent source (highest elevation), nor are there extensive associated low-radar-return, fine-grained deposits attributable to deposition by an eruption plume. Given the high atmospheric pressure, even very explosive volcanic events are unable to ballistically deposit coarse debris over distances of more than approximately 1 km (Fagents and Wilson, 1995). The much longer run-out distances of the bright halo

deposits (50–100 km) implies a ground-hugging flow regime, though the magmatic properties required to sustain an eruption column during deposition have not been established.

With the exception of Mead crater, the impact craters within the quadrangle appear to postdate the formation of the regional plains and the major corona flow units; we do not observe partially buried craters such as Gautier and Heloise craters in the Bell Regio quadrangle (V–9). Mead crater postdates the formation of the regional plains (unit pr) but may predate the emplacement of some corona-related flows (unit fc). Later flows from the corona complex and sources to the north and east of the crater embay the distal ejecta of Mead but do not appear to be the source of the enigmatic low-emissivity material that forms the crater floor.

Fine-grained materials that smooth the surface and reduce the backscattered radar echo mantle large areas in the eastern and southeastern portions of the quadrangle, and at least some component of this debris is readily moved by the regional winds. We attribute this mantling material to impact comminution or melting of the target rock, but its mode of emplacement differs with location. Many such deposits have feathery edges and tend to drape local topography. In at least some areas, however, the radar-dark material appears to behave as a fluid, exhibiting lobate margins and control by subtle topographic features. Given the large volume of impact-generated debris expected for a crater like Mead, such behavior may be analogous to that of basin-related light plains on the Moon (for example, Howard and others, 1974). We infer that the radar-dark mantling material was initially much more extensive and is being progressively stripped from high-standing terrain and redeposited in local depressions.

Given the lack of stratigraphic contacts between Bell and eastern Eistla Regiones, inferences of their relative age are speculative. Studies of western Eistla and Bell Regiones imply a common progression of volcanic landforms with inferred increasing lithospheric thickness at Venusian rises (Campbell and Rogers, 1994; McGill, 1998). As hypothesized, the early stage of the rise is characterized by hot, thin lithosphere that permits rapid eruption of rising magma and the development of annular tectonic deformation patterns (coronae). Over time, the crust thickens, trapping magma at depth, with more infrequent eruptions producing steeper constructs (for example, Tepev Mons in V–9 and Gula Mons in V–20) and rougher flows.

The gravity signature of eastern Eistla Regio and Nefertiti Corona in Bell Regio (V–9) suggests ongoing dynamic support for these features in contrast to the compensated topography of Nyx and Tepev Montes (V–9; Zimmerman and Johnson, 2000). The lack of major shield volcanoes in eastern Eistla Regio may thus be attributed to several scenarios: (1) eastern Eistla Regio is younger than Bell Regio; (2) the supply of magma waned prior to development of steep-sided constructs; or (3) the mechanism of plume rise and eruption differs between the two regions. Our geologic mapping cannot differentiate between these possibilities, though the presence of uncompensated topography supports scenarios (1) or (3) over (2).

ACKNOWLEDGMENTS

This work was funded, in part, by a grant from the National Aeronautics and Space Administration (NASA) Planetary Geology and Geophysics Program. The authors thank A.K. Johnston and C.M. Fortezzo for assistance with the digital mapping. Comments by D.A. Young, K.L. Tanaka, and an anonymous reviewer were very helpful in revising the text and map.

REFERENCES CITED

Basilevsky, A.T., and Head, J.W., 1998, The geologic history of Venus—A stratigraphic view: Journal of Geophysical Research, v. 103, p. 8531–8544.

Bilotti, F., and Suppe, J., 1999, The global distribution of wrinkle ridges on Venus: Icarus, v. 139, p. 137–159.

Campbell, B.A., 1994, Merging Magellan emissivity and SAR data for analysis of Venus surface dielectric properties: Icarus, v. 112, p. 187–203.

———1995, Use and interpretation of Magellan quantitative data in Venus mapping: U.S. Geological Survey Open-File Report 95–519.

———1999, Surface formation rates and impact crater densities on Venus: Journal of Geophysical Research, v. 104, p. 21,951–21,956.

Campbell, B.A., and Campbell, P.G., 2002, Geologic map of the Bell Regio (V–9) quadrangle, Venus: U.S. Geological Survey Geologic Investigations Series I–2743, scale 1:5,000,000.

Campbell, B.A., Campbell, D.B., and DeVries, C., 1999, Surface processes in the Venus highlands—Results from analysis of Magellan and Arecibo data: Journal of Geophysical Research, v. 104, p. 1897–1916.

Campbell, B.A., Glaze, L., and Rogers, P.G., 1998, Pyroclastic deposits on Venus—Remote-sensing evidence and modes of formation [abs.], *in* Lunar and Planetary Science Conference, 29th, March 16–20, 1998: Houston, Tex., Lunar and Planetary Institute [CD-ROM].

Campbell, B.A., and Rogers, P.G., 1994, Bell Regio, Venus—Integration of remote sensing data and terrestrial analogs for geologic analysis: Journal of Geophysical Research, v. 99, p. 21,153–21,171.

Copp, D.L., Guest, J.E., and Stofan, E.R., 1998, New insights into Corona evolution—Mapping on Venus: Journal of Geophysical Research, v. 103, p. 19,401–19,417.

Fagents, S.A., and Wilson, L., 1995, Explosive volcanism on Venus—Transient volcanic explosions as a mechanism for localized pyroclast dispersal: Journal of Geophysical Research, v. 100, p. 26,327–26,338.

Ford, P.G., and Pettengill, G.H., 1992, Venus topography and kilometer-scale slopes: Journal of Geophysical Research, v. 97, p. 13,103–13,114.

Guest, J.E., and Stofan, E.R., 1999, A new view of the stratigraphic history of Venus: Icarus, v. 139, p. 55–66.

Herrick, R.R., and Sharpton, V.L., 1996, Geologic History of

the Mead impact basin: Geology, v. 24, p. 11–14.
Howard, K.A., Wilhelms, D.E., and Scott, D.H., 1974, Lunar basin formation and highland stratigraphy: Reviews of Geophysics and Space Physics, v. 12, p. 309–327.
McGill, G.E., 1994, Hotspot evolution and Venusian tectonic style: Journal of Geophysical Research, v. 99, p. 23,149–23,161.
———1998, Central Eistla Regio, Origin and relative age of topographic rise: Journal of Geophysical Research, v. 103, p. 5889–5896.
———2000, Geologic map of the Sappho Patera quadrangle (V–20), Venus: U.S Geological Survey Geologic Investigations Series I–2637, scale 1:5,000,000.
Rogers, P.G., and Zuber, M.T., 1998, Tectonic evolution of Bell Regio, Venus—Regional stress, lithospheric flexure, and edifice stresses: Journal of Geophysical Research, v. 103, p. 16,841–16,853.
Schaber, G.G., Strom, R.G., Moore, H.J., Soderblom, L.A., Kirk, R.L., Chadwick, D.J., Dawson, D.D., Gaddis, L.R., Boyce, J.M., and Russell, J., 1992, Geology and distribution of impact craters on Venus—What are they telling us?: Journal of Geophysical Research, v. 97, p. 13,257–13,302.
Stofan, E.R., Sharpton, V.L., Schubert, G., Baer, G., Bindschadler, D.L., Janes, D.M., and Squyres, S.W., 1992, Global distribution and characteristics of coronae and related features on Venus—Implications for origin and relation to mantle processes: Journal of Geophysical Research, v. 97, p. 13,347–13,378.
Weitz, C.M., 1993, Impact Craters, *in* Guide to Magellan Data Interpretation: Jet Propulsion Laboratory Publication 93–24, p. 75–92.
Zimmerman, S.B., and Johnson, C.L., 2000, Gravity signatures of coronae on Venus—Implications for models for corona formation and evolution: Eos (American Geophysical Union, Transactions), v. 81, p. S300.

Table 1. *Ancillary data for selected map units within the Mead quadrangle (V–21), Venus*

[The table presents image location, average values for incidence angle (ι), planetary radius, HH-polarization backscatter coefficient (σ_o), rms slope (θ_{rms}), Fresnel normal reflectivity (ρ_o), horizontal polarization emissivity (E_H), and calculated bounds on the surface dielectric constant using smooth (ε_s) and rough (ε_r) surface cases (Campbell, 1994, 1995). Where Cycle 3 stereo images are available, these data provide a second incidence angle for each unit. Some mapped units are omitted where the microwave properties could not be meaningfully presented as a single value (for example, crater ejecta)]

Unit label	Location (deg)	Incidence angle, ι (deg)	Radius (km)	Backscatter, σ_o (dB)	Root-mean-square slope, θ_{rms} (deg)	Fresnel reflectivity, ρ_o	Emissivity, E_H	Dielectric constant ε_s, ε_r
fN3	22.63–22.88 N. 47.97–48.38 E.	25 44	6050.86	–5.1 –8.3	6.1	0.081	0.897	2.4, 3.5
fN1	26.29–26.67 N. 50.30–51.55 E.	43	6051.95	–17.5	0.80	0.106	0.843	3.3, 5.1
fK	9.09–9.72 N. 30.17–31.05 E.	46	6051.86	–20.7	2.1	0.119	0.804	3.8, 6.4
fD	0.09–1.10 N. 33.01–33.77 E.	45	6052.40	–18.2	2.8	0.195	0.814	3.7, 6.0
fP	2.59–3.15 N. 44.51–45.06 E.	46	6051.91	–19.1	2.1	0.174	0.821	3.5, 5.8
fc	16.84–17.65 N. 39.02–39.73 E.	26 45	6052.50	–13.5 –20.4	1.7	0.122	0.806	5.6, 6.6
fC	5.87–6.26 N. 44.32–44.79 E.	46	6051.12	–15.8	1.7	0.067	0.875	2.6, 4.0
fM	0.00–1.00 N. 49.5–50.5 E.	45	6051.64	–17.6	1.2	0.096	0.843	3.2, 5.0
hb	16.84–16.99 N. 36.69–36.89 E.	26 45	6053.04	–5.3 –8.2	4.2	0.123	0.864	4.0, 4.7
phO	4.31–4.93 N. 54.65–55.41 E.	25 46	6051.41	–12.6 –18.1	1.4	0.116	0.827	3.4, 5.5
phB	24.0–24.5 N. 31.5–32.0 E.	44	6051.41	–16.9	3.6	0.087	0.878	2.7, 4.0
pr	4.67–6.36 N. 30.69–31.90 E.	46	6051.36	–16.6	2.9	0.091	0.853	3.0, 4.7
t	0.62–1.72 N. 55.45–56.31 E.	25 45	6052.72	–7.8 –13.5	6.3	0.078	0.856	3.0, 4.6